Soft Matter

PAPER

View Article Online
View Journal | View Issue

Cite this: *Soft Matter*, 2024, **20**, 3620

Novel turbulence and coarsening arrest in active-scalar fluids

Nadia Bihari Padhan, * Kolluru Venkata Kiran and Rahul Pandit

We uncover a new type of turbulence – activity-induced homogeneous and isotropic turbulence – in a model that has been employed to investigate motility-induced phase separation (MIPS) in a system of microswimmers. The active Cahn–Hilliard–Navier–Stokes (CHNS) equations, also called active model H, provide a natural theoretical framework for our study. In this CHNS model, a single scalar order parameter ϕ, positive (negative) in regions of high (low) microswimmer density, is coupled with the velocity field $\boldsymbol{u}$. The activity of the microswimmers is governed by an activity parameter ζ that is positive for extensile swimmers and negative for contractile swimmers. With extensile swimmers, this system undergoes complete phase separation, which is similar to that in binary-fluid mixtures. By carrying out pseudospectral direct numerical simulations (DNSs), we show, for the first time, that (a) this model develops an emergent nonequilibrium, but statistically steady, state (NESS) of active turbulence, for the case of contractile swimmers, if ζ is sufficiently large and negative, and (b) this turbulence arrests the phase separation. We quantify this suppression by showing how the coarsening-arrest length scale does not grow indefinitely, with time t, but saturates at a finite value at large times. We characterise the statistical properties of this active-scalar turbulence by employing energy spectra and fluxes and the spectrum of ϕ. For sufficiently high Reynolds numbers, the energy spectrum $\mathcal{E}(k)$ displays an inertial range, with a power-law dependence on the wavenumber k. We demonstrate that, in this range, the flux $\Pi(k)$ assumes a nearly constant, negative value, which indicates that the system shows an inverse cascade of energy, even though energy injection occurs over a wide range of wavenumbers in our active-CHNS model.

Received 1st February 2024,
Accepted 3rd April 2024

DOI: 10.1039/d4sm00163j

rsc.li/soft-matter-journal

1 Introduction

Active turbulence, spatiotemporal chaos in active-matter systems [see, *e.g.*, ref. 1–4], has garnered considerable attention over the past decade. This intriguing form of turbulence manifests itself in various experimental systems, including bacterial suspensions,[1,5–11] suspensions of microtubules, and molecular motors.[12,13] In classical-fluid turbulence, a nonequilibrium statistically steady state (NESS) is reached when the fluid is driven by an external force; by contrast, in active fluids, the microscopic constituents drive the system by converting chemical sources of energy into kinetic energy.[5,14] Many studies have focused on understanding emergent turbulence-type patterns by using continuum hydrodynamical models, in which phenomenological parameters depend on the microscopic details of the active fluid. An overview of the various models can be found in ref. 3. In certain models, the energy spectrum of such turbulence exhibits universal power-law behaviors.[4,15] In contrast, there are instances in which power-law exponents for these energy spectra depend on parameters in the model.[7,11,16] The elucidation of the statistical properties of these types of emergent turbulent states continues to be an important challenge in active-matter research. Recent studies have shown the importance of fluid inertia in some systems that display active turbulence such as active polar and nematic fluids [see, *e.g.*, ref. 17–20]. In addition, considerable attention has been directed towards the study of scalar active fluids, in which the intricate spatiotemporal evolution of an active fluid arises from the interaction of a scalar order parameter ϕ with the fluid velocity $\boldsymbol{u}$. Scalar active fluids are simpler than their polar or nematic counterparts, yet they are rich enough to yield intriguing emergent NESSs,[21–23] and they have been used in studying active droplets[24] and active stratified turbulence.[25]

We uncover a new type of turbulence – activity-induced homogeneous and isotropic turbulence in a model that has been employed to investigate motility-induced phase separation (MIPS)[22,24] in a system of microswimmers. MIPS is a fascinating emergent phenomenon, in which an initially uniform state of active swimmers undergoes spontaneous separation into dense and dilute phases due to persistent motion and repulsion. The active Cahn–Hilliard–Navier–Stokes (CHNS)

Centre for Condensed Matter Theory, Department of Physics, Indian Institute of Science, Bangalore, 560012, India. E-mail: nadia@iisc.ac.in

equations, also known as the active model H,[22] provide a natural theoretical framework for our study.

The active model H describes MIPS, in wet or momentum-conserving fluids, an emergent phenomenon that is relevant for spherical colloidal swimmers;[22,26,27] MIPS does not rely on alignment interactions, so it can be described by a scalar field without the direct use of polar or nematic fields. In this CHNS model, a single scalar order parameter ϕ [which is positive (negative) in regions where the microswimmer density is high (low)] is coupled with the velocity field $\boldsymbol{u}$. The activity of the microswimmers is governed by an activity parameter ζ that is positive for extensile swimmers and negative for contractile swimmers. With extensile swimmers, this system undergoes complete phase separation, which is similar to that in binary-fluid mixtures.[22] By carrying out pseudospectral direct numerical simulations (DNSs), we show, for the first time, that this model develops an emergent nonequilibrium, but statistically steady, state (NESS) of active turbulence, for the case of contractile swimmers, if ζ is sufficiently large and negative. This turbulence arrests the phase separation into regions with positive and negative values of ϕ, in much the same way as conventional fluid turbulence leads to the suppression of phase separation in a binary-fluid mixture.[28–30] We quantify this suppression by showing how the coarsening-arrest length scale does not grow indefinitely, with time t, but saturates at a finite value at large times. We then characterise the statistical properties of this active-scalar turbulence by employing the energy spectrum and fluxes, which are familiar from classical fluid turbulence, and also the spectrum of ϕ, which is used in studies of phase separation. For sufficiently high Reynolds numbers, the energy spectrum $\mathscr{E}(k)$ displays an inertial range, with a power-law dependence on the wavenumber k. We demonstrate that, in this range, the flux $\Pi(k)$ assumes a nearly constant, negative value, which indicates that the system shows an inverse cascade of energy that is similar to its counterpart in 2D homogeneous and isotropic fluid turbulence, even though energy injection occurs over a wide range of wavenumbers in our active-CHNS model.

The remaining part of this paper is organised as follows. Section 2 introduces the active CHNS model, summarises the numerical methods we employ to study it, and defines the statistical measures we use to characterise active turbulence in this model. In Section 3 we present the results of our study. We discuss the significance of our results in Section 4.

2 Model, methods, and statistical measures

We introduce the active-CHNS model in Section 2.1. In Section 2.2, we describe the statistical measures we use to characterise active turbulence in this model. Finally, in Section 2.3 we give the details of our pseudospectral DNS.

2.1 The active Cahn–Hilliard–Navier–Stokes model

We consider the incompressible active CHNS equations (also called active model H) to study active turbulence in systems of contractile swimmers[22,24] in two spatial dimensions (2D):

$$\partial_t\phi + (\boldsymbol{u}\cdot\nabla)\phi = M\nabla^2\left(\frac{\delta\mathscr{F}}{\delta\phi}\right); \tag{1}$$

$$\partial_t\omega + (\boldsymbol{u}\cdot\nabla)\omega = \nu\nabla^2\omega + \frac{3}{2}\varepsilon\nabla\times(\nabla\cdot\boldsymbol{\Sigma}^{\mathrm{A}}) - \alpha\omega; \tag{2}$$

$$\nabla\cdot\boldsymbol{u} = 0; \tag{3}$$

where $\omega = [\nabla\times\boldsymbol{u}]\cdot\hat{e}_z$ is the vorticity field; ν, α, and M are the kinematic viscosity, bottom friction, and mobility, respectively.

We write eqn (2) in the vorticity-streamfunction formulation by introducing the stream function $\psi(\boldsymbol{x},t)$ such that $\boldsymbol{u} = (\partial_y\psi, -\partial_x\psi)$ and $\omega = -\nabla^2\psi$. This formulation, which has been used extensively for studying two-dimensional fluid turbulence and the fluid dynamics of binary- and ternary-fluid mixtures,[24,29,31–33] offers a distinct advantage in two dimensions because the vorticity is a (pseudo)scalar. $\mathscr{F}$ is the Landau–Ginzburg variational free-energy functional given by

$$\mathscr{F}[\phi,\nabla\phi] = \int_\Omega\left[\frac{3}{16}\frac{\sigma}{\varepsilon}\left(\phi^2-1\right)^2 + \frac{3}{4}\sigma\varepsilon|\nabla\phi|^2\right], \tag{4}$$

in which the first term is a double-well potential with minima at $\phi = \pm1$. The scalar order parameter ϕ is positive (negative) in regions where the microswimmer density is high (low); in the interfaces between these regions, ϕ varies smoothly, over a width ε. The free-energy penalty for an interface is given by the bare surface tension σ. In the inherently nonequilibrium active model H, all terms in the stress tensor do not follow from $\mathscr{F}$. In particular, we must include the stress tensor $\boldsymbol{\Sigma}^{\mathrm{A}}$, which has the form of a nonlinear Burnett term and has the components:[22,24,25,34]

$$\boldsymbol{\Sigma}^{\mathrm{A}}_{ij} = -\zeta\left[\partial_i\phi\partial_j\phi - \frac{\delta_{ij}}{2}|\nabla\phi|^2\right], \tag{5}$$

where ζ, the activity coefficient,† can take both positive and negative values: $\zeta < 0$ ($\zeta > 0$) for contractile (extensile) swimmers.[22] The tensor $\boldsymbol{\Sigma}^{\mathrm{A}}$, which is symmetric and traceless, resembles the stress tensor, used in the passive model H where $\zeta = \sigma$.[22,35,36] The microswimmers exhibiting contractile behavior are prone to orienting perpendicular to an interface rather than parallel to it. When $\zeta < 0$, the active force $\nabla\cdot\boldsymbol{\Sigma}^{\mathrm{A}}$ acts as an effective negative surface force in the Navier–Stokes equations and yields arrested MIPS.

2.2 Statistical characterisation

To characterise the statistical properties of active-scalar turbulence, we employ energy spectra and fluxes, which are familiar from classical fluid turbulence, and the spectrum of ϕ. These quantities not only help us to understand, *via* DNS, the emergent turbulent like behaviour (characterized by spatiotemporal fluctuations) in eqn (1)–(3), but they also aid us in differentiating active scalar turbulence from classical 2D incompressible

† The activity coefficient is an effective contribution to the stress tensor in eqn (5) and can be written as $\zeta = \sigma + \zeta'$, where ζ' and σ are the active and passive contributions to the stress term in eqn (5).[22]

Table 1 The values of various parameters in our DNS runs R1–R9. The following parameters are fixed in all these runs: $N = 1024$, grid size $dx = 2\pi/N$, $\varepsilon = 3dx$, $L = 2\pi$, $\mathrm{Cn} = 3dx/L$, $M = \varepsilon^2/2$, $\sigma = 1$, $\nu = 5 \times 10^{-3}$, and $\alpha = 0.01$

Run	$\lvert\zeta\rvert$	$\mathrm{Re}_{L_\mathrm{I}}$	α'	Pe	We
R1	0	0	—	0	0
R2	0.001	1.1×10^{0}	5.6×10^{-2}	2.8×10^{-1}	1.6×10^{-4}
R3	0.01	3.2×10^{0}	7.9×10^{-3}	8.5×10^{-1}	2.3×10^{-3}
R4	0.03	1.3×10^{1}	6.6×10^{-3}	3.5×10^{0}	2×10^{-2}
R5	0.05	4.3×10^{1}	7.8×10^{-3}	1.2×10^{1}	1.1×10^{-1}
R6	0.1	6.9×10^{1}	7.0×10^{-3}	1.9×10^{1}	2.3×10^{-1}
R7	0.5	1.1×10^{2}	5.8×10^{-3}	3.2×10^{1}	5.3×10^{-1}
R8	1	1.2×10^{2}	6.8×10^{-3}	3.3×10^{1}	5.8×10^{-1}
R9	1.5	1.3×10^{2}	5.7×10^{-3}	3.4×10^{1}	6.1×10^{-1}

fluid turbulence [see, *e.g.*, ref. 31 and 37–39] and also turbulent patterns found in other active systems [see, *e.g.*, ref. 17–20]. We define the shell-averaged energy and phase-field spectra, respectively, both at time t and averaged over time [the time average is denoted by $\langle\cdot\rangle_t$]:

$$\begin{aligned} \mathscr{E}(k,t) &\equiv \sum_{k\le k'<k+1} |\hat{\boldsymbol{u}}(\boldsymbol{k}',t)|^2; \quad \Phi(k,t) \equiv \sum_{k\le k'<k+1} |\hat{\phi}(\boldsymbol{k}',t)|^2; \\ \mathscr{E}(k) &\equiv \langle \mathscr{E}(k,t)\rangle_t; \quad \Phi(k) \equiv \langle \Phi(k,t)\rangle_t; \end{aligned} \tag{6}$$

the caret denotes a spatial Fourier transform. Our CHNS study of active scalar turbulence uses the Reynolds, Péclet, Weber, Cahn, and the non-dimensional friction numbers that are, respectively:

$$\begin{aligned} \mathrm{Re} &= \frac{L_\mathrm{I} u_\mathrm{rms}}{\nu}; \quad \mathrm{Pe} = \frac{\varepsilon L_\mathrm{I} u_\mathrm{rms}}{M\sigma}; \\ \mathrm{We} &= \frac{L_\mathrm{I} {u_\mathrm{rms}}^2}{\sigma}; \quad \mathrm{Cn} = \varepsilon/L; \quad \alpha' = \frac{\alpha L_\mathrm{I}}{u_\mathrm{rms}}; \end{aligned} \tag{7}$$

where u_rms and L_I are, respectively, the root-mean-squared velocity and the fluid integral length scale; L is the length of the side of the simulation domain; and $\mathscr{L}(t)$ and L_c are the time-dependent and mean coarsening length scales; these are defined as follows:

$$\begin{aligned} u_\mathrm{rms} &= \left[\sum_k \mathscr{E}(k)\right]^{1/2}; \quad L_\mathrm{I} = 2\pi \frac{\sum_k \mathscr{E}(k)}{\sum_k k\mathscr{E}(k)}; \\ \mathscr{L}(t) &= \frac{\sum_k \Phi(k,t)}{\sum_k k\Phi(k,t)}; \quad L_\mathrm{c} = \langle \mathscr{L}(t)\rangle_t. \end{aligned} \tag{8}$$

In Table 1, we provide the non-dimensional parameters from our direct numerical simulations (DNSs) for various values of the activity parameter $|\zeta|$. Furthermore, $\mathscr{E}(k,t)$ satisfies the following energy-budget equation:[30,40,41]

$$\partial_t \mathscr{E}(k,t) = T(k,t) + D_\alpha(k,t) + D_\nu(k,t) + S^\phi(k,t), \tag{9}$$

where

$$\begin{aligned} T(k,t) &= -\Re\left[\sum_{k\le|\boldsymbol{k}'|<k+1} [\hat{\boldsymbol{u}}(-\boldsymbol{k}',t)\cdot\boldsymbol{P}(\boldsymbol{k}')\cdot(\widehat{\boldsymbol{u}\cdot\nabla\boldsymbol{u}})(\boldsymbol{k}',t)]\right]; \\ D_\alpha(k,t) &= -2\alpha\mathscr{E}(k,t), \quad D_\nu(k,t) = -2\nu k^2\mathscr{E}(k,t), \\ S^\phi(k,t) &= \Re\left[\sum_{k\le|\boldsymbol{k}'|<k+1} [\hat{\boldsymbol{u}}(-\boldsymbol{k}',t)\cdot\boldsymbol{P}(\boldsymbol{k}')\cdot(\widehat{\nabla\cdot\boldsymbol{\Sigma}^\mathrm{A}})(\boldsymbol{k}',t)]\right] \end{aligned} \tag{10}$$

are, respectively, the energy transfer because of the inertial term, the energy dissipations arising from friction and the viscosity, and the energy transfer *via* the active-stress term; the transverse projector $\boldsymbol{P}(\boldsymbol{k})$, which enforces the incompressibility condition, has the components $P_{ij} \equiv (\delta_{ij} - k_i k_j/k^2)$. We also use the following mean energy transfers from the inertial, friction, viscous, and active-stress terms, and the associated kinetic-energy and active-stress fluxes:[41]

$$\begin{aligned} T(k) &= \langle T(k,t)\rangle_t; \quad S^\phi(k) = \left\langle S^\phi(k,t)\right\rangle_t; \\ D_\alpha(k) &= \langle D_\alpha(k,t)\rangle_t; \quad D_\nu(k) = \langle D_\nu(k,t)\rangle_t; \\ \Pi(k) &= -\int_0^{k'} T(k')\mathrm{d}k'; \quad \Pi^\phi(k) = -\int_0^{k'} S^\phi(k')\mathrm{d}k'. \end{aligned} \tag{11}$$

2.3 Direct numerical simulations

We carry out DNSs of the active-CHNS partial differential equations [eqn (1)–(5)] by using the pseudospectral method[24,29,32,42] in a 2D periodic square domain, $\mathscr{D} \equiv [0,L]^2$, with L being the length of the side of the square. We evaluate spatial derivatives in the Fourier space and the nonlinear terms in the physical space. For time integration, we use the semi-implicit exponential-time-difference Runge–Kutta 2 (ETDRK2) method.[43] We employ the 1/2-dealiasing scheme to remove the Fourier aliasing errors.[24,29,32,42] To resolve the interface of width ε, we ensure that there are three grid points across the interface. We use a CUDA-C code that we have developed and optimised for an NVIDIA A100 processor.

2.4 Initial conditions

We use the following initial conditions for the ω and ϕ fields:

$$\omega(x,y,0) = 0; \quad \phi(x,y,0) = \phi_0 + \xi(x,y); \tag{12}$$

where $\xi(x,y)$, a random number distributed uniformly on the interval $[-0.1,0.1]$, provides a random perturbation to the $\phi = \phi_0 = 0$ state.

3 Results

In this section, we present a series of DNSs that we have designed to demonstrate how the activity of contractile swimmers [$\zeta < 0$ in eqn (5)] leads to active turbulence that is strong enough to suppress motility-induced phase separation. Our results are the

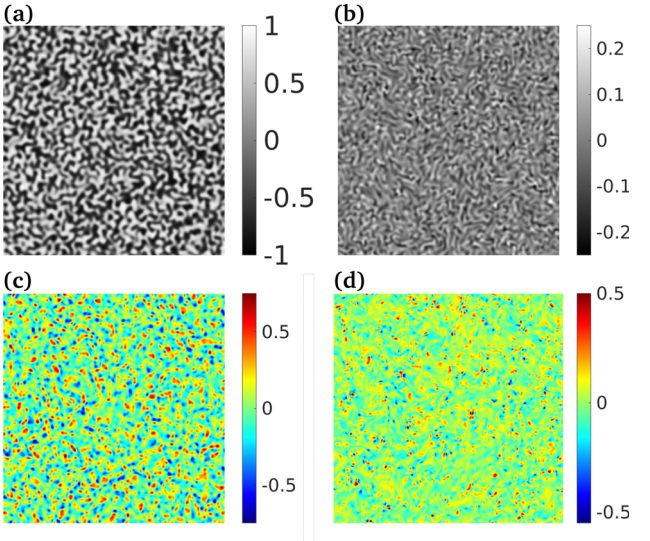

Fig. 1 Pseudo-grayscale plots of the ϕ field [at representative times in the nonequilibrium statistically steady state (NESS)] for the activity parameter (a) $|\zeta|$ = 0.01 and (b) $|\zeta|$ = 1.5. Pseudocolor plots of the vorticity field, normalized by the maximum of $|\omega|$, are shown in (c) and (d) for the parameters in (a) and (b), respectively.

active-turbulence counterparts of the suppression of phase separation (also called coarsening arrest) by fluid turbulence [see, *e.g.*, ref. 28 and 29].

We note that, if the activity $\zeta = 0$, the stress tensor (5) vanishes, so the coupled equations [eqn (1)–(5)] decouple into Cahn–Hilliard equations or model B[35,44] and the Navier–Stokes equations[45–47] for a Newtonian fluid; the advection term for the ϕ field is set to zero by virtue of the initial conditions. Therefore, the domain growth or coarsening takes place solely *via* diffusion, without hydrodynamical effects, and it follows the well-established Lifshitz–Slyozov domain-growth form $\mathscr{L}(t) \sim t^{1/3}$ [see, *e.g.*, ref. 44, 48 and 49]; complete phase separation also occurs for extensile swimmers[22] that lead to $\zeta > 0$. When $\zeta = \sigma$, the active model H presented in eqn (1)–(5) converges to the passive model H, which has been utilized for studying spinodal decomposition in binary fluid mixtures.[28,29]

We concentrate on active-turbulence-induced suppression of phase separation and the diffusive Lifshitz–Slyozov coarsening in our model [eqn (1)–(5)] with contractile swimmers, for which the activity parameter $\zeta < 0$.‡ Active turbulence and coarsening arrest in the active-CHNS model [eqn (1)–(5)] can be visualized qualitatively by using pseudo-gray-scale plots of the ϕ field as we show in Fig. 1(a) and (b) for $|\zeta| = 0.01$ and $|\zeta| = 1.5$, respectively, at representative times in the nonequilibrium statistically steady state (NESS). We illustrate the kinetic energy density $E(t) = \sum_k \mathscr{E}(k,t)$ in Fig. 2(c) to demonstrate that the system has reached the NESS. In Fig. 1(c) and (d), we present the pseudocolor plots of the vorticity field, normalized by the maximum of $|\omega|$, for the parameters in Fig. 1(a) and (b), respectively. These plots show clearly that the typical size of a single-phase domain decreases as activity-induced turbulence is enhanced by an increase in the value of $|\zeta|$.

We quantify active-turbulence-induced suppression of phase separation by plotting the coarsening length scale $\mathscr{L}(t)$ *versus* time t in Fig. 2(a) for various values of $|\zeta|$; the plot for $\zeta = 0$ shows growth that is consistent with the Lifshitz–Slyozov form $\mathscr{L}(t) \sim t^{1/3}$ (dashed line§). As t increases, $\mathscr{L}(t)$ saturates to a finite value for $|\zeta| > 0$, *i.e.*, eqn (1)–(5) lead to coarsening-arrest because of active turbulence. In Fig. 2(b) we show how the mean coarsening-arrest scale $L_c = \langle \mathscr{L}(t) \rangle_t$ decreases as $|\zeta|$ increases (red curve); the attendant growth of the integral-scale Reynolds number Re_{L_I} (blue curve) signals the enhancement of activity-induced turbulence.

We now characterise the statistical properties of activity-induced turbulence in eqn (1)–(5). We begin with the log–log plots of compensated energy and scalar-ϕ spectra, $k^{5/3}\mathscr{E}(k)$ and $k^{-\delta}\Phi(k)$, *versus* k, in Fig. 3(a) and (b), respectively, for various values of $|\zeta|$, with a fit $\delta \simeq 1.17 \simeq 7/6$ [the error bars on the exponents are comparable to the symbol sizes (see the insets of Fig. 3)]. These plots suggest that, as ζ increases, the activity-induced turbulence in this system leads to a nonequilibrium statistically steady state (NESS) with an inertial range of scales in which the energy spectrum has a power-law form that is consistent with $\mathscr{E}(k) \sim k^{-5/3}$. We show below that this power-law spectrum arises because of an inverse cascade of energy. Its power-law form can then be surmised as in statistically steady homogeneous and isotropic 2D-fluid turbulence with an inverse energy cascade.[31,37–39] Note that this power-law region extends over nearly one-and-a-half decades of k at the largest value $|\zeta|(= 1.5)$ that we consider.

We examine the energy-transfer mechanisms in the NESS of activity-induced turbulence in eqn (1)–(5) by using the energy-budget equation [eqn (9)] and evaluating the relevant scale-by-scale energy contributions.[30,40,41] In Fig. 4(a) and (b), we present, for the illustrative values $|\zeta| = 0.001$ and $|\zeta| = 1.5$, respectively, plots *versus* k (log scale) of the inertial, friction, viscous, and active-stress contributions $T(k)$ (red), $D_\alpha(k)$ (purple), $D_\nu(k)$ (yellow) and $S^\phi(k)$ (blue), which we have defined in eqn (11). Such plots indicate that, for low values of $|\zeta|$, the contributions of $T(k)$ and $D_\alpha(k)$ are negligible [Fig. 4(a)], so, in the NESS with $\langle \partial_t \mathscr{E}(k,t) \rangle_t = 0$, dominant balance yields $D_\nu(k) + S^\phi(k) = 0$. As $|\zeta|$ increases, both $T(k)$ and $D_\alpha(k)$ increase in magnitude [Fig. 4(b)], so a four-term balance is required in the NESS.

To show that activity-induced turbulence exhibits a *bona fide* inertial range, we present plots for $|\zeta| = 0.001$, 0.01, 0.1, and 1.5 of the energy flux $\Pi(k)$ [eqn (11)] *versus* k (log scale) [Fig. 5(a)]. We also present log–log plots *versus* k of $|\Pi(k)|$ [Fig. 5(b)] and $\Pi^\phi(k)$ [Fig. 5(c)]. These plots show constant fluxes over at least one decade of the wavenumber k, so we have a well-defined inertial range that has a remarkable similarity to fluid turbulence.[50] The sign of $\Pi(k)$ in this range of scale indicates

‡ At low inertia, motility-induced phase separation is also suppressed in this model.[22]

§ In any DNS in a finite domain, $\mathscr{L}(t)$ approaches a finite value that is comparable to the linear size of the domain.

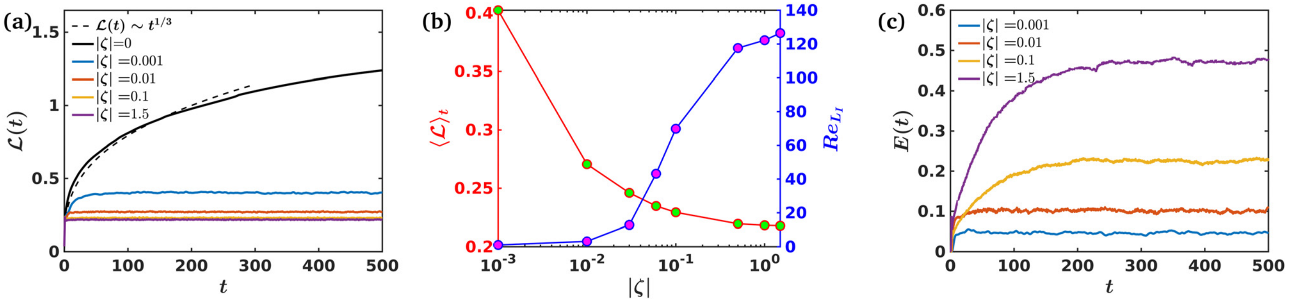

Fig. 2 (a) Plot of the coarsening length scale $\mathscr{L}(t)$ [eqn (8)] *versus* time t for various values of $|\zeta|$; the plot for $\zeta = 0$ shows growth that is consistent with the Lifshitz–Slyozov form $\mathscr{L}(t) \sim t^{1/3}$ (dashed line); (t) saturates to a finite value for $|\zeta| > 0$. (b) log-linear plots of the mean coarsening-arrest scale $L_c = \langle \mathscr{L}(t) \rangle_t$ (red curve) and the integral-scale Reynolds number Re_{L_I} (blue curve) *versus* $|\zeta|$. (c) Plots of the kinetic energy density $E(t)$ *versus* time t for various values of $|\zeta|$. The plots are displaced vertically for ease of visualization.

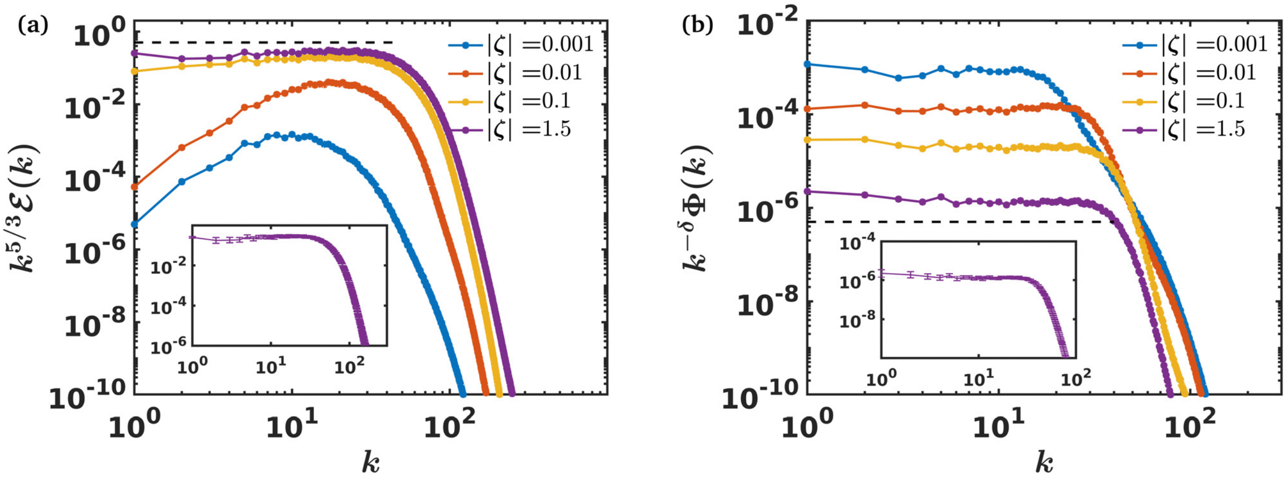

Fig. 3 log–log plots *versus* the wavenumber k of spectra for $|\zeta| = 0.001, 0.01, 0.1, 1.5$: (a) the compensated energy spectrum $k^{5/3}\mathscr{E}(k)$. For $|\zeta| = 0.1, 1.5$, the exponent is $-5/3$ (black dotted line in the compensated spectrum). (b) The compensated phase-field spectrum $k^{-\delta}\Phi(k)$ for $|\zeta| = 0.001, 0.01, 0.1, 1.5$. These spectra show the power-law behaviour $\Phi(k) \sim k^{\delta}$ (black dotted line in the compensated spectrum), where $\delta \simeq 1.17 \simeq 7/6$. The insets in (a) and (b) indicate that the error bars on the exponents $-5/3$ and $7/6$ are comparable to the symbol sizes.

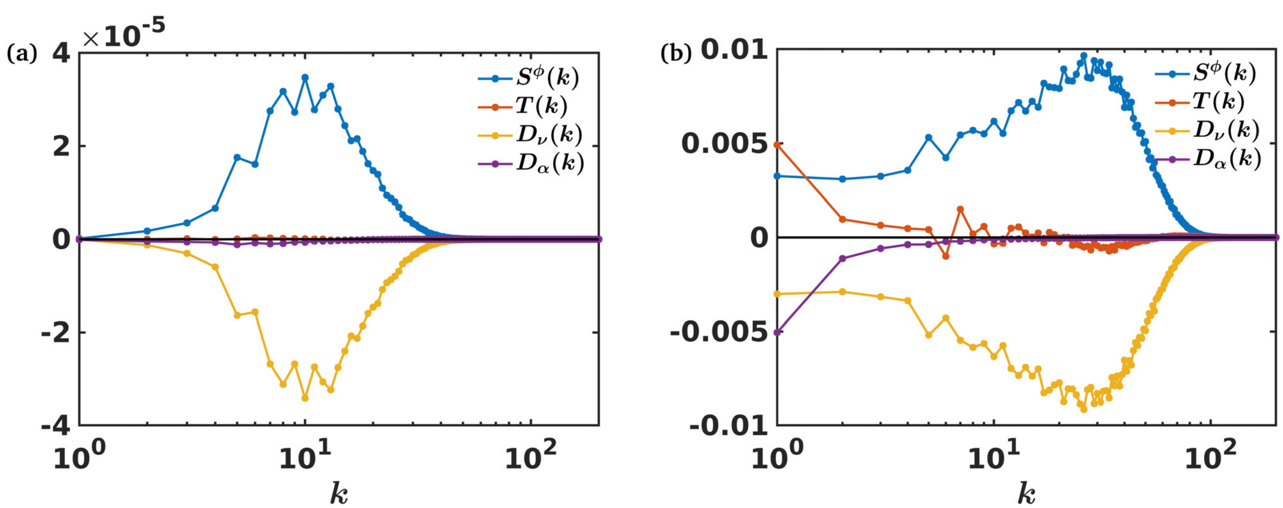

Fig. 4 Plots *versus* k (log scale) of the contributions $T(k)$, $D_\alpha(k)$, $D_\nu(k)$, and $S^\phi(k)$ [eqn (11)], in red, purple, yellow, and blue, respectively, for (a) $|\zeta| = 0.001$ and (b) $|\zeta| = 1.5$.

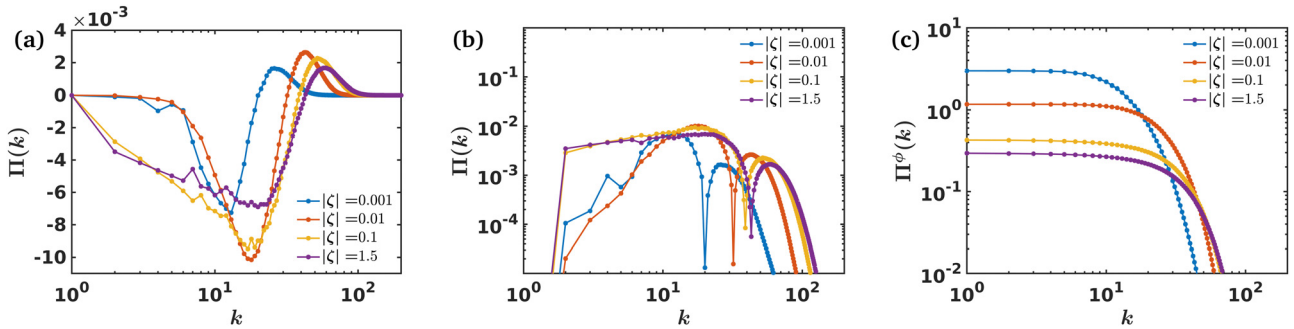

Fig. 5 Plots for $|\zeta|$ = 0.001, 0.01, 0.1, and 1.5 of the normalized (a) energy flux $\Pi(k)L_I/u_{rms}^3$ *versus* k (log scale) and log–log plots *versus* k of (b) $|\Pi(k)|L_I/u_{rms}^3$ and (c) $\Pi^\phi(k)L_I/u_{rms}^3$.

that activity-induced turbulence in eqn (1)–(5) yields an inverse cascade of energy that is reminiscent of a similar cascade in 2D statistically steady homogeneous and isotropic fluid turbulence.[31,37–39] By comparing the different plots in Fig. 5(a), we see that this inverse cascade is suppressed as $|\zeta|$ decreases; this is reminiscent of similar cascade suppression in instability-driven 2D turbulence.[51]

4 Conclusions

We have uncovered activity-induced homogeneous and isotropic turbulence in the active Cahn–Hilliard–Navier–Stokes (CHNS) equations, which provide a natural theoretical framework for our study, in which a single scalar order parameter ϕ [positive (negative) in regions where the microswimmer density is high (low)] is coupled with the velocity field $\boldsymbol{u}$. The activity of the microswimmers is governed by an activity parameter ζ that is positive for extensile swimmers and negative for contractile swimmers [see eqn (1)–(5)]. With extensile swimmers, this system undergoes complete phase separation, as in binary-fluid mixtures.[22] By carrying out extensive pseudospectral direct numerical simulations (DNSs), we have shown that this model develops an emergent nonequilibrium, but statistically steady, state (NESS) of active turbulence, for the case of contractile swimmers, if ζ is sufficiently large and negative. This turbulence arrests the phase separation into regions with positive and negative values of ϕ, as in conventional fluid turbulence leads to the suppression of phase separation in a binary-fluid mixture.[28–30] Our investigations provide the first observation and characterization of turbulence within an active-matter system that is undergoing arrested motility-induced phase separation.

We have quantified this suppression by showing how the coarsening-arrest length $\mathscr{L}(t)$ scale does not grow indefinitely, with time t, but saturates at a finite value at large times. We have then characterised the statistical properties of this active-scalar turbulence by employing the energy spectrum $\mathscr{E}(k)$ and the fluxes $\Pi(k)$ and $\Pi^\phi(k)$. We have also obtained the spectrum of ϕ, which is used in studies of phase separation. For sufficiently high Reynolds numbers, we have shown that the energy spectrum $\mathscr{E}(k)$ displays an inertial range, with a power-law dependence on the wavenumber k. We have demonstrated that, in this range, the flux $\Pi(k)$ assumes a nearly constant, negative value, which indicates that the system shows an inverse cascade of energy that is similar to its counterpart in 2D homogeneous and isotropic fluid turbulence, even though energy injection occurs over a wide range of wavenumbers in our active-CHNS model.

Our statistical characterization of active-CHNS turbulence shows that it is fundamentally different from conventional 2D fluid turbulence,[31,37] forced 2D CHNS turbulence,[29] and other types of active-fluid turbulence, discussed, *e.g.*, in ref. 1–11 and 25. For large values of $|\zeta|$, active-CHNS turbulence has some similarities to conventional 2D fluid turbulence and 2D forced CHNS turbulence, inasmuch as it shows an inverse-cascade region with $\mathscr{E}(k) \sim k^{-5/3}$. The $|\zeta|$-dependent, small-k, power-law regime in $\mathscr{E}(k)$ is qualitatively reminiscent of parameter-dependent small-k power-law regimes in energy-spectra in some minimal models for bacterial turbulence.[3,4,7–9,11,16] The scalar spectrum $\Phi(k)$ of active-CHNS turbulence shows a substantial power-law regime which is different from that in conventional forced 2D CHNS turbulence.[29] It might be possible to develop an EDQNM-type closure for both the energy and the scalar spectra; such a closure might lead to scaling ranges in $\mathscr{E}(k)$ and $\Phi(k)$ and values for the exponents that characterize these scaling ranges. The development of such a closure analysis lies beyond the scope of the current paper. The fluxes and energy budgets in active-CHNS turbulence are also markedly different from their counterparts in other types of 2D turbulence. Our study investigates the effects of active-CHNS turbulence that is distinct from the suppression of motility-induced phase separation in the active model H[22] with external noise.

We hope, therefore, that our active-CHNS study will lead to investigations of experimental realisations of this system. Our results are of potential relevance to systems of contractile swimmers, *e.g.*, *Chlamydomonas reinhardtii*[52,53] and synthetic active colloids,[54,55] such as Janus particles, with particles that exhibit dominant propulsion on the front hemisphere and, therefore, function as pullers.[26,27,56,57] We look forward to the experimental verification of our results, especially in the former system, where it should be possible to control the activity by changing the oxygen concentration in low-light conditions.

Author contributions

NBP, KVK, and RP planned the research and analysed the numerical data; NBP and KVK carried out the calculations and prepared the tables, figures, and the draft of the manuscript; NBP, KVK, and RP revised the manuscript in detail and approved the final version.

Conflicts of interest

No conflicts of interests, financial or otherwise, are declared by the authors.

Acknowledgements

We thank the Science and Engineering Research Board (SERB) and the National Supercomputing Mission (NSM), India for support, and the Supercomputer Education and Research Centre (IISc) for computational resources.

Notes and references

1 H. H. Wensink, J. Dunkel, S. Heidenreich, K. Drescher, R. E. Goldstein, H. Löwen and J. M. Yeomans, *Proc. Natl. Acad. Sci. U. S. A.*, 2012, **109**, 14308–14313.
2 K. Qi, E. Westphal, G. Gompper and R. G. Winkler, *Commun. Phys.*, 2022, **5**, 49.
3 R. Alert, J. Casademunt and J.-F. Joanny, *Annu. Rev. Condens. Matter Phys.*, 2022, **13**, 143–170.
4 S. Mukherjee, R. K. Singh, M. James and S. S. Ray, *Nat. Phys.*, 2023, 1–7.
5 J. Dunkel, S. Heidenreich, K. Drescher, H. H. Wensink, M. Bär and R. E. Goldstein, *Phys. Rev. Lett.*, 2013, **110**, 228102.
6 A. Kaiser, A. Peshkov, A. Sokolov, B. Ten Hagen, H. Löwen and I. S. Aranson, *Phys. Rev. Lett.*, 2014, **112**, 158101.
7 A. Joy, *et al.*, *Phys. Rev. Fluids*, 2020, **5**, 024302.
8 M. Linkmann, G. Boffetta, M. C. Marchetti and B. Eckhardt, *Phys. Rev. Lett.*, 2019, **122**, 214503.
9 M. Linkmann, M. C. Marchetti, G. Boffetta and B. Eckhardt, *Phys. Rev. E*, 2020, **101**, 022609.
10 I. S. Aranson, *Rep. Prog. Phys.*, 2022, **85**, 076601.
11 K. V. Kiran, A. Gupta, A. K. Verma and R. Pandit, *Phys. Rev. Fluids*, 2023, **8**, 023102.
12 A. Opathalage, M. M. Norton, M. P. Juniper, B. Langeslay, S. A. Aghvami, S. Fraden and Z. Dogic, *Proc. Natl. Acad. Sci. U. S. A.*, 2019, **116**, 4788–4797.
13 K.-T. Wu, J. B. Hishamunda, D. T. Chen, S. J. DeCamp, Y.-W. Chang, A. Fernández-Nieves, S. Fraden and Z. Dogic, *Science*, 2017, **355**, eaal1979.
14 J. Dunkel, S. Heidenreich, M. Bär and R. E. Goldstein, *New J. Phys.*, 2013, **15**, 045016.
15 R. Alert, J.-F. Joanny and J. Casademunt, *Nat. Phys.*, 2020, **16**, 682–688.
16 V. Bratanov, F. Jenko and E. Frey, *Proc. Natl. Acad. Sci. U. S. A.*, 2015, **112**, 15048–15053.
17 S. P. Thampi, R. Golestanian and J. M. Yeomans, *Phys. Rev. Lett.*, 2013, **111**, 118101.
18 S. P. Thampi, R. Golestanian and J. M. Yeomans, *Philos. Trans. R. Soc., A*, 2014, **372**, 20130366.
19 R. Chatterjee, N. Rana, R. A. Simha, P. Perlekar and S. Ramaswamy, *Phys. Rev. X*, 2021, **11**, 031063.
20 C. Rorai, F. Toschi and I. Pagonabarraga, *Phys. Rev. Lett.*, 2022, **129**, 218001.
21 S. Saha, J. Agudo-Canalejo and R. Golestanian, *Phys. Rev. X*, 2020, **10**, 041009.
22 A. Tiribocchi, R. Wittkowski, D. Marenduzzo and M. E. Cates, *Phys. Rev. Lett.*, 2015, **115**, 188302.
23 T. Frohoff-Hülsmann, U. Thiele and L. M. Pismen, *Philos. Trans. R. Soc., A*, 2023, **381**, 20220087.
24 N. B. Padhan and R. Pandit, *Phys. Rev. Res.*, 2023, **5**, L032013.
25 J. Bhattacharjee and T. Kirkpatrick, *Phys. Rev. Fluids*, 2022, **7**, 034602.
26 A. Nsamela, A. I. Garcia Zintzun, T. D. Montenegro-Johnson and J. Simmchen, *Small*, 2023, **19**, 2202685.
27 M. Popescu, W. Uspal, Z. Eskandari, M. Tasinkevych and S. Dietrich, *Eur. Phys. J. E: Soft Matter Biol. Phys.*, 2018, **41**, 1–24.
28 P. Perlekar, R. Benzi, H. J. Clercx, D. R. Nelson and F. Toschi, *Phys. Rev. Lett.*, 2014, **112**, 014502.
29 P. Perlekar, N. Pal and R. Pandit, *Sci. Rep.*, 2017, **7**, 44589.
30 P. Perlekar, *J. Fluid Mech.*, 2019, **873**, 459–474.
31 G. Boffetta and R. E. Ecke, *Annu. Rev. Fluid Mech.*, 2012, **44**, 427–451.
32 N. Pal, P. Perlekar, A. Gupta and R. Pandit, *Phys. Rev. E*, 2016, **93**, 063115.
33 N. B. Padhan and R. Pandit, *Phys. Fluids*, 2023, **35**, 112105.
34 A. Das, J. Bhattacharjee and T. Kirkpatrick, *Phys. Rev. E*, 2020, **101**, 023103.
35 P. C. Hohenberg and B. I. Halperin, *Rev. Mod. Phys.*, 1977, **49**, 435.
36 M. E. Cates and E. Tjhung, *J. Fluid Mech.*, 2018, **836**, P1.
37 R. Pandit, D. Banerjee, A. Bhatnagar, M. Brachet, A. Gupta, D. Mitra, N. Pal, P. Perlekar, S. S. Ray, V. Shukla and D. Vincenzi, *Phys. Fluids*, 2017, **29**, 111112.
38 R. H. Kraichnan, *Phys. Fluids*, 1967, **10**, 1417–1423.
39 R. H. Kraichnan and D. Montgomery, *Rep. Prog. Phys.*, 1980, **43**, 547.
40 A. Alexakis and L. Biferale, *Phys. Rep.*, 2018, **767**, 1–101.
41 M. K. Verma, *Energy transfers in fluid flows: multiscale and spectral perspectives*, Cambridge University Press, 2019.
42 C. Canuto, M. Y. Hussaini, A. Quarteroni and A. Thomas Jr, *et al.*, *Spectral methods in fluid dynamics*, Springer Science Business Media, 2012.
43 S. M. Cox and P. C. Matthews, *J. Comput. Phys.*, 2002, **176**, 430–455.
44 S. Puri, *Kinetics of phase transitions*, CRC Press, 2009, pp. 13–74.
45 C. Navier, Mémoires de l'Académie Royale des Sciences de l'Institut de France, 1823, vol. 6, pp. 389–440.
46 G. G. Stokes, *Mathematical and physical papers*, 1901, vol. 3.

47 C. R. Doering and J. D. Gibbon, *Applied analysis of the Navier-Stokes equations*, Cambridge University Press, 1995.
48 I. M. Lifshitz and V. V. Slyozov, *J. Phys. Chem. Solids*, 1961, **19**, 35–50.
49 A. J. Bray, *Adv. Phys.*, 2002, **51**, 481–587.
50 U. Frisch, *Turbulence: the legacy of AN Kolmogorov*, Cambridge University Press, 1995.
51 A. van Kan, B. Favier, K. Julien and E. Knobloch, *J. Fluid Mech.*, 2022, **952**, R4.
52 J. M. Yeomans, D. O. Pushkin and H. Shum, *Eur. Phys. J.: Spec. Top.*, 2014, **223**, 1771–1785.
53 A. A. Fragkopoulos, J. Vachier, J. Frey, F.-M. Le Menn, M. G. Mazza, M. Wilczek, D. Zwicker and O. Baumchen, *J. R. Soc., Interface*, 2021, **18**, 20210553.
54 A. Zöttl and H. Stark, *J. Phys.: Condens. Matter*, 2016, **28**, 253001.
55 J. R. Howse, R. A. Jones, A. J. Ryan, T. Gough, R. Vafabakhsh and R. Golestanian, *Phys. Rev. Lett.*, 2007, **99**, 048102.
56 P. Sharan, Z. Xiao, V. Mancuso, W. E. Uspal and J. Simmchen, *ACS Nano*, 2022, **16**, 4599–4608.
57 S. Michelin and E. Lauga, *Sci. Rep.*, 2017, **7**, 42264.